Evolution of a BHBH binary system in an accretion disk + dark matter spike environment

Nicole Grillo

March 2024

1 Introduction

We model a binary system embedded in an accretion disk, along with a dark matter spike and gravitational waves emission.The goal for our modelization is to produce an estimate of the following quantity:

$$\dot{r} = \dot{r}_{\text{gas}} + \dot{r}_{\text{DF}} + \dot{r}_{\text{GW}}, \tag{1}$$

where $\dot{r}_{\text{gas}}$ is the contribution coming from gas torques from the accretion disk surrounding the binary, $\dot{r}_{\text{DF}}$ is the effect of dynamical friction from the presence of the dark matter spike, and $\dot{r}_{\text{GW}}$ is the contribution from the gravitational waves emission. Specifically, we adopt the classical Newtonian formalism, computing the results from the reduced mass-system, and in case assuming *later* that $m_1 \gg m_2$.

Once the shape of $\dot{r}$ is clear, one can evaluate the phase of the binary system from a generic f-frequency to the f_{isco}-frequency. Assuming circular orbits the frequency is:

$$f = \frac{1}{\pi}\sqrt{\frac{G(m_1 + m_2)}{r^3}}. \tag{2}$$

We can evaluate $\Phi(f)$ as:

$$\Phi(f) = 2\pi \int_f^{f_{\text{isco}}} \frac{dt}{df'} f' df', \tag{3}$$

where the relation $\frac{dt}{df'}$ is extracted directly from the expression in Equation 1 by the following chain rule: $\frac{dr}{dt}\frac{df}{dr} = \frac{df}{dt}$. In this formalism we have that $\Phi_{\text{isco}}(f) = \int_{f_{\text{isco}}}^{f_{\text{isco}}} \frac{dt}{df'} f' df' = 0$. We introduce the **dephasing** as the phase difference between the vacuum case (GW-only), and any of the combined environments (it could even be just one):

$$\Delta\Phi = \Phi(f) - \Phi_{\text{env}}(f), \tag{4}$$

The number of cycles before merger then becomes:
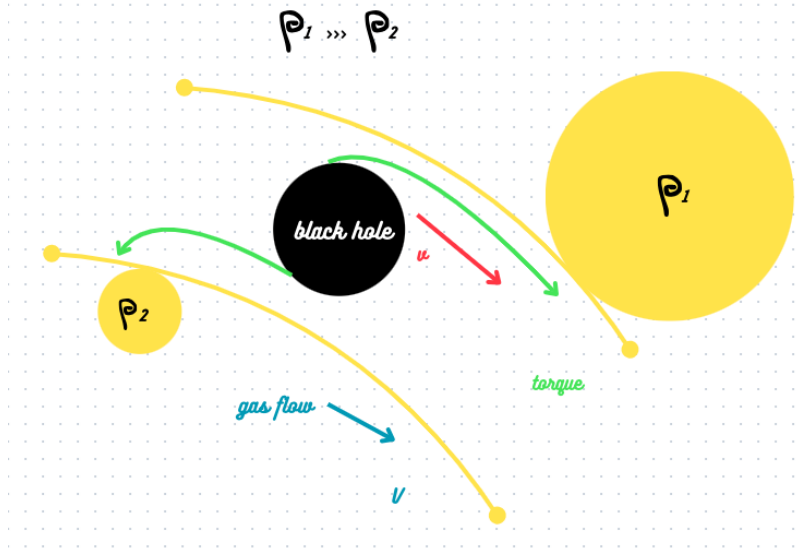
$$N_{\text{cycles}} = \frac{\Delta\Phi}{2\pi} \tag{5}$$

Figure 1: Inward torque from gas (D being the bigger density of gas particles, d the smaller), acting on the moving secondary black hole. The unbalance in density exerts a stronger "outward" pull on the gas moved by the black hole, and a torque arises as a result of this pull (blue line in the plot). The black hole moves closer to the center.

If we set a sensible threshold on the number of cycles we are able to observe, we can state whether the environment is recognized from the data or not:

$$N_{\text{cycles}} \geq 1 \tag{6}$$

2 Modelling $\dot{r}$

2.1 Torques from the Disk

We model the torque from accretion disks assuming only gas torques acting on the binary. The inspiral will be influenced so that it becomes faster in time when gas torques are present. The process and equations are very similar to type I migration of planets. The general take home message is the following: in the case of accretion disks, it is instead the perturbation of the disk due to the companion object which leads to an asymmetric build up of particles on smaller or larger radii than the orbit of the companion object. These particles then back-react on the black hole and impart gas torques which can either speed up the inspiral (if the build up of particles is on larger radii than the companion) or slow it down (if the build up of particles is on smaller radii). A very rough, simple sketch is seen in Figure 1, and Figure 2.

2.1.1 Formalism

We assume the disk to follow a surface density profile:

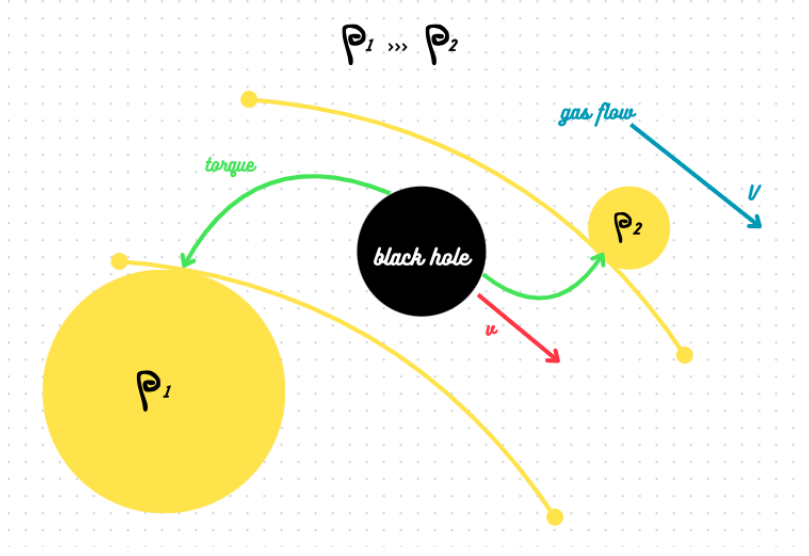$$\Sigma(r) = \Sigma_0 \left(\frac{r}{r_0} \right)^{\alpha}, \tag{7}$$

Figure 2: Outward torque from gas (D being the bigger density of gas particles, d the smaller), acting on the moving secondary black hole. The unbalance in density exerts a stronger "inward" pull on the gas moved by the black hole, and a torque arises as a result of this pull (blue line in the plot). The black hole moves away from the center.

with Σ_0 and r_0 arbitrary normalization constants. We work in the Newtonian limit, and we consider only circular Keplerian orbits.

The torque acting on the gas can be expressed using the formulation we find in [Derdzinski et al., 2020] and [Tanaka et al., 2002]:

$$T_{\text{gas}} = \Sigma(r)r^4\Omega^2 q^2 \mathcal{M}^2, \tag{8}$$

where $\Sigma(r)$ is from Equation 7, Ω is the angular velocity, which we assume Keplerian, q is the mass ratio of the binary, and $\mathcal{M}$ is the Mach number. In the Newtonian formalism, the following relation holds:

$$m_1 + m_2 = \frac{1}{G}rv^2, \tag{9}$$

with $r = r_1 + r_2$ being the separation, and $v = v_1 + v_2$ the total velocity. The angular momentum L is:

$$L = \mu v r = \mu\sqrt{G(m_1 + m_2)r}. \tag{10}$$

Taking the time derivative of Equation 10 we obtain:

$$\dot{L} = \frac{\mu}{2}\sqrt{\frac{G(m_1 + m_2)}{r}}\dot{r}. \tag{11}$$

Thus, knowing that $\dot{L} = T_{\text{gas}}$ by definition, we can link $\dot{r}$ to the torque effect by the gas:

$$\dot{r} = \dot{r}_{\text{gas}} = -2\Sigma_0 \frac{r^{\gamma+3/2}}{r_0^\gamma}\frac{G^{1/2}(m_1 + m_2)^{1/2}}{\mu}q^2 \mathcal{M}^2. \tag{12}$$

Note that the expression can be further simplified in the case where $m_1 \gg m_2$.

2.2 Dark matter spike

We model the effect of dark matter as dynamical friction. This drag results from the black hole accelerating dark matter particles (assumed to be cold and collisionless) in its wake – thus increasing their energy and momentum. As a consequence of the conservation of energy and momentum, the satellite itself must therefore lose energy/momentum and slow down. Over time, this causes the binary to inspiral much faster than in vacuum. Figure 3 should give an idea of the drag effect by the wake of particles exerting the friction on the moving black hole.

2.2.1 Formalism

We model the dark matter spike with a power law as in [Cole et al., 2023]:

$$\rho_{\text{CDM}} = \rho_6 \left(\frac{r_6}{r} \right)^{\gamma_{\text{s}}}, \tag{13}$$

where, again, ρ_6 and r_6 are reference values. We assume dynamical friction to be the only effect at play, and model the force acting on the binary as in [Chandrasekhar, 1943]:

$$F_{\text{df}} = -\frac{4\pi G^2 \mu^2 \log(\Lambda)\rho(r)\xi(v)}{v^2}, \tag{14}$$

where $\xi(v)$ is the fraction of DM particles that move *slower* than μ, in the assumption that the faster ones are not influenced by the passage of the black hole.

The variation of the angular momentum is given by the following relation $dL/dt = -F_{\text{DF}}r$ from [Binney and Tremaine, 1987], which translates into:

$$\dot{L} = \frac{4\pi G^2 \mu^2 \log(\Lambda)\rho_6 r_6^{\gamma_s}\xi(v)}{v^2 r^{\gamma_s - 1}} \overset{(11)}{=} \frac{\mu}{2}\sqrt{\frac{G(m_1 + m_2)}{r}}\dot{r}. \tag{15}$$

Thus, we can find $\dot{r}_{\text{DF}}$ as:

$$\dot{r} = \dot{r}_{\text{DF}} = -\frac{8\pi G^{\frac{1}{2}} \mu \log(\Lambda)\rho_6 r_6^{\gamma_s}\xi(v)}{r^{\gamma_s - \frac{5}{2}}(m_1 + m_2)^{\frac{3}{2}}}. \tag{16}$$

It is important to note that up to this point we considered the density profile of the dark matter to be constant over time. However, if we do so, it largely overestimates the effect on the inspiral of the binary system. Indeed, $\rho(r) = \rho(r, t)$ will evolve in time as much as r. In [Kavanagh et al., 2020] they studied the equations leading to evolve the density profile in time, assuming:

- The orbital elements evolve on a timescale that is long compared to the orbital period. This allows them to set the rate of energy being injected into the halo as constant over a small number of orbits.

- The equilibration timescale for the DM halo is much shorter than the timescale for the secular evolution of the system, thus allowing them to compute the new equilibrium density profile of the DM 'instantaneously' after energy is injected.

- The DM halo is spherically symmetric and isotropic, and remains so throughout the evolution of the system.
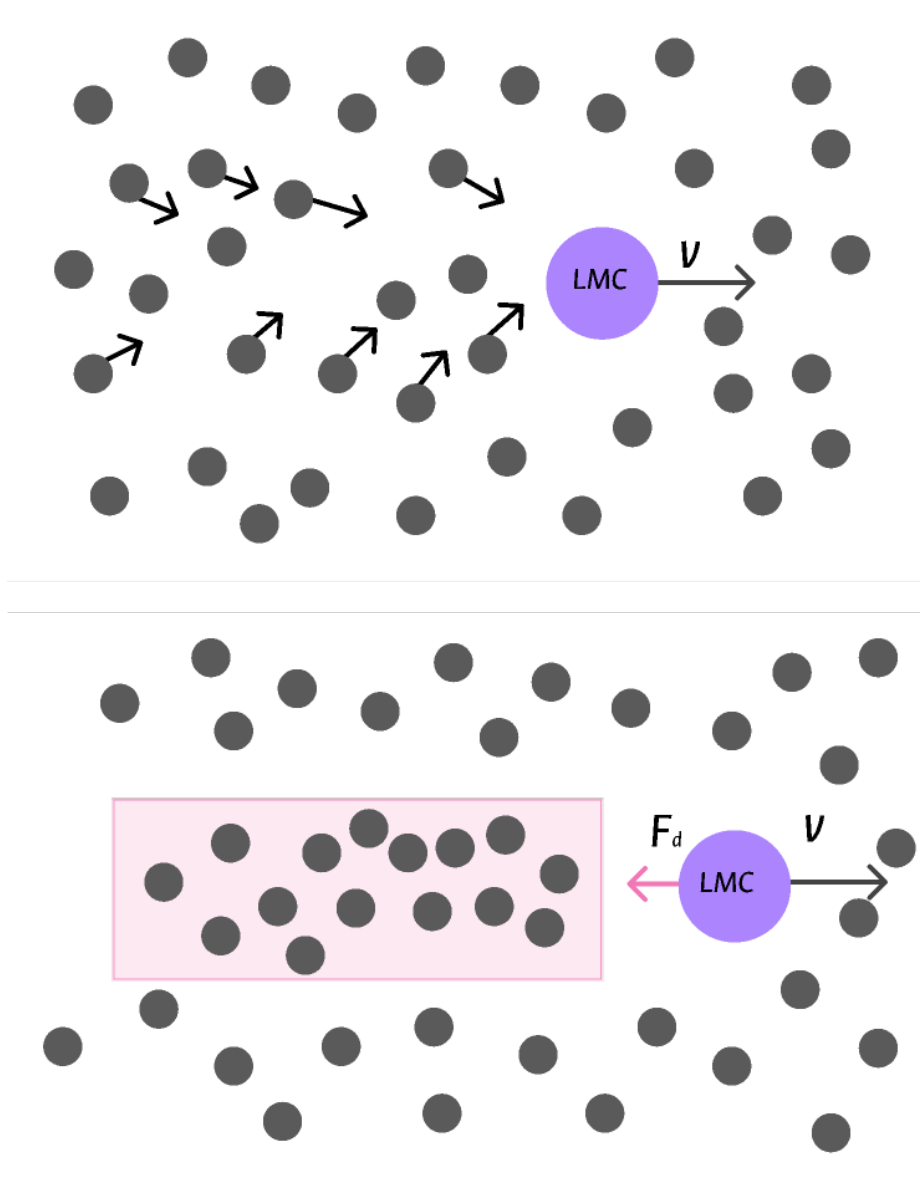
Figure 3: A simple sketch of the effect of dynamical friction onto a moving body in the DM halo.

They describe the spike with with an equilibrium phase space distribution function $f = f(\epsilon)$ that depends only on the relative energy per unit mass. The general idea is that if one can study the evolution of the distribution function f, then they can self-consistently evolve the DM halo along with the binary and reconstruct the density profile. They define $P_\epsilon(\Delta\epsilon)$ as the probability (over a single orbit) that a particle with energy ϵ scatters with the compact object and gains an energy $\Delta\epsilon$. Assuming that the evolution of the system is much slower than the orbital frequency, one can write $\Delta f \simeq T_{\text{orb}} \partial f / \partial t$, with $T_{\text{orb}} = 2\pi\sqrt{r^3/GM}$, so that:

$$T_{\text{orb}} \frac{\partial f}{\partial t} = -p_\epsilon \cdot f(\epsilon, t) + \int \left(\frac{\epsilon}{\epsilon - \Delta\epsilon}\right)^{\frac{5}{2}} f(\epsilon - \Delta\epsilon, t) P_{\epsilon - \Delta\epsilon}(\Delta\epsilon) d\Delta\epsilon. \tag{17}$$

One can then evolve the distribution function over a number of orbits (assuming that the binary separation changes slowly compared to the orbital period). Evaluating the $P_\epsilon(\Delta\epsilon)$, one has all the ingredients to evolve the function. The system then reads:

$$\begin{cases} \frac{dr(t)}{dt} = F_1 \left[r, \left[\int d^3 v f(\epsilon, t; r) \right] \right] \\ \frac{\partial f(\epsilon, t; r)}{\partial t} = F_2 \left[f(\epsilon, t; r), \int d\Delta\epsilon f(\epsilon - \Delta\epsilon, t; r) \right], \end{cases} \tag{18}$$

with F_1, F_2 being functionals depending on the quantities we saw above. The density profile at a given time will be the density distribution integrated over the velocities:

$$\rho(r, t) = 4\pi \int_0^{v_{\max}} v^2 f\left(\Psi(r) - \frac{1}{2}v^2, t\right) dv. \tag{19}$$

One is then able to solve numerically Equation 18, and Equation 16 and produce a solution every time iteration. The code to do so is in this link `https://github.com/bradkav/HaloFeedback/blob/master/HaloFeedback.py`.

2.2.2 The effective profile

Once we have an integration describing the density profile of the dark matter spike, we can fit the solution simply, considering the "average" displacement of dark matter particles caused by the passage of the binary over multiple orbital periods.

We start by defining a very useful constant that will come in handy:

$$c_f = \frac{5c^5}{8m_1^2} \pi^{\frac{2(\gamma_s - 4)}{3}} G^{-\frac{2+\gamma_s}{3}} (m_1 + m_2)^{\frac{1-\gamma_s}{3}} r_6^{\gamma_s} \xi \rho_6 \log\Lambda \tag{20}$$

The result, which is also the one adopted by [Cole et al., 2023], describes directly the final phase solution as:

$$\Phi(f) = \Phi(f)_{\text{GW}} \left\{ 1 - \eta y^{-\lambda} (1 - 2F_1(1, \theta, 1 + \theta, -y^{-\frac{5}{3\theta}})) \right\} \begin{cases} \theta = \frac{5}{\gamma_e} \\ \lambda = \frac{11 - 2(\gamma_s + \gamma_e)}{3} \\ \eta = \frac{5 + 2\gamma_e}{2(8 - \gamma_s)} \left(\frac{f_{eq}}{f_b}\right)^{\frac{11 - 2\gamma_s}{3}} \\ f_t = f_b \end{cases} \tag{21}$$

We fixed $\gamma_e = 5/2$, $f_{eq} = c_f^{\frac{3}{11 - 2\gamma_s}}$, and

$$f_b = \beta\left(\frac{m_1}{1000 M_\odot}\right)^{-\alpha_1}\left(\frac{m_2}{M_\odot}\right)^{\alpha_2}\left[1 + \zeta \log\left(\frac{\gamma_s}{\gamma_r}\right)\right] \begin{cases} \alpha_1 = 1.4412 \\ \alpha_2 = 0.4511 \\ \beta = 0.8163 \text{ Hz} \\ \zeta = -0.4971 \\ \gamma_r = 1.4396 \end{cases} \tag{22}$$

If we want to extract the related $\dot{r}_{\text{eff}}$ to revert the process and possibly add the contribution to the whole set of environments we follow the below passages:

1. Find the quantity $\frac{d\Phi(f)}{df}$;

2. Find $\frac{df}{dt} = \frac{2\pi f \, df}{d\Phi(f)}$ from the definition of phase;

3. Find $\dot{r}_{\text{eff,dm}}$ using this formula: $\dot{r}_{\text{eff,dm}} = \frac{df}{dt} \cdot \frac{df}{dr}^{-1}$, where $\frac{df}{dr}$ comes from Equation 2.

The phase derivative reads:

$$\begin{aligned}
\frac{d\Phi(f)}{df} = \frac{d\Phi(f)_{\text{GW}}}{df} &- \eta\Big(\frac{d\Phi(f)_{\text{GW}}}{df}y^{-\lambda}\cdot(1 - 2F_1(1,\theta,1+\theta,-y^{-\frac{5}{3\theta}}))+ \\
&- \frac{\lambda}{y}\frac{dy}{df}\cdot y^{-\lambda}(1 - 2F_1(1,\theta,1+\theta,-y^{-\frac{5}{3\theta}}))\Phi(f)_{\text{GW}}+ \\
&+ \Phi(f)_{\text{GW}}y^{-\lambda} * (-\frac{d(2F_1)}{df}\frac{dy}{df})\Big),
\end{aligned} \tag{23}$$

where I substituted the analytical form of the $\Phi(f)_{\text{GW}}$ (found in Section 3, Equation 34), so that:

$$\frac{d\Phi(f)_{\text{GW}}}{df} = \frac{-G^{-\frac{5}{3}}(M)^{\frac{1}{3}}c^5}{16\pi^{\frac{5}{3}}m_1 m_2)(-\frac{5}{3})(f^{(-\frac{5}{3}-1)})}, \tag{24}$$

and $\frac{d(2F_1)}{df}$, which is the derivative of the gaussian hyperfunction with respect to the frequency. In my code, I used a simple differentiation method:

$$\frac{d(2F_1)}{df}\Big|_i = \frac{2F_{1,i+1} - 2F_{1,i}}{f_{i+1} - f_i} \tag{25}$$

2.3 Gravitational waves

We now want to find the power per unit area carried away by the gravitational wave as expressed by the time-average of the gravitational radiation Poynting vector. As the system loses energy to gravitational waves, the binaries spiral in towards each other, increasing their orbital angular frequency, which leads to enhanced gravitational wave energy loss.

One can calculate the energy loss by GW in analogy with the electromagnetism case, and find that it is:

$$\frac{dE_{\text{GW}}}{dt} = \frac{32G^4(m_1 + m_2)(m_1 m_2)^2}{5(cr)^5}. \tag{26}$$

The energy of the binary system can be calculated from simple Newtonian considerations on the total energy:

$$E_{\mathrm{BS}} = -\frac{Gm_1 m_2}{2r}. \tag{27}$$

We derive the Equation 27 in time, and set it equal to the gravitational waves-driven loss of energy of Equation 26, assuming this is the only energy loss from the system.

$$\frac{dE_{\mathrm{BS}}}{dt} = \frac{Gm_1 m_2}{2r^2}\dot{r}, \tag{28}$$

$$\downarrow$$

$$\dot{r} = \dot{r}_{\mathrm{GW}} = -\frac{64(m_1 + m_2)G^3 m_1 m_2}{5c^5 r^3}. \tag{29}$$

Finally, we can rewrite Equation 1 with the complete form of $\dot{r}_{\mathrm{gas}}$, $\dot{r}_{\mathrm{DM}}$, and $\dot{r}_{\mathrm{GW}}$.

$$\dot{r} = -2\Sigma_0 \frac{r^{\gamma+3/2}}{r_0^{\gamma}} \frac{G^{1/2}(m_1+m_2)^{1/2}}{\mu} q^2 \mathcal{M}^2 - \frac{8\pi G^{\frac{1}{2}} \mu \log{(\Lambda)}\rho_6 r_6^{\gamma_s} \xi(v)}{r^{\gamma_s - \frac{5}{2}}(m_1+m_2)^{\frac{3}{2}}} + \\ -\frac{64(m_1+m_2)G^3 m_1 m_2}{5c^5 r^3}. \tag{30}$$

This last equation is (at least to the first order) approximating the change in the radial separation between the two objects in the binary over time.

3 Extracting $\Phi(f)$ in vacuum (GW only)

We already have the shape of $f(r)$ from Equation 2, so that we can write:

$$\frac{df}{dr} = \frac{1}{\pi}(-\frac{3}{2})\sqrt{\frac{G(m_1+m_2)}{r^5}}. \tag{31}$$

We will also need the inverse $r(f)$, to substitute in Equation 3:

$$r(f) = \sqrt[3]{\frac{G(m_1+m_2)}{\pi^2 f^2}} = \tilde{c} f^{-\frac{2}{3}}, \tag{32}$$

with $\tilde{c} = \sqrt[3]{\frac{G(m_1+m_2)}{\pi^2}}$. From now on I will adopt $m_1 + m_2 = M$. Making use of Equation 29, we can write:

$$\frac{df}{dt} = \frac{dr}{dt}\frac{df}{dr} = \left(\frac{32}{5}\frac{G^3 M m_1 m_2}{c^5 r^3}\right)\cdot\left(\frac{1}{\pi}\frac{3}{2}\sqrt{\frac{GM}{r^5}}\right) = \tilde{k} r^{-\frac{11}{2}}, \tag{33}$$

where I used $\tilde{k} = \frac{96}{5\pi}\frac{M^{\frac{3}{2}}(m_1 m_2)G^{\frac{7}{2}}}{c^5}$. Finally, the phase $\Phi(f)$ reads:

$$\Phi(f) \stackrel{(3)}{=} \int_f^{f_{\text{isco}}} \frac{1}{\tilde{k}} r^{\frac{11}{2}} f' df' \stackrel{(32)}{=} \int_f^{f_{\text{isco}}} \frac{\tilde{c}^{\frac{11}{2}}}{\tilde{k}} f'^{-\frac{11 \cdot 2}{2 \cdot 3}} f' df' =$$

$$\int_f^{f_{\text{isco}}} \frac{\tilde{c}^{\frac{11}{2}}}{\tilde{k}} f'^{-\frac{8}{3}} df' = -\frac{3}{5} \frac{\tilde{c}^{\frac{11}{2}}}{\tilde{k}} (f'^{-\frac{5}{3}}) \Big|_f^{f_{\text{isco}}}. \tag{34}$$

Substituting the expressions for $\tilde{c}$ and $\tilde{k}$ we finally obtain:

$$\Phi(f) = \frac{G^{-\frac{5}{3}} M^{\frac{1}{3}} c^5}{32 \pi^{\frac{8}{3}} m_1 m_2} (f^{-\frac{5}{3}} - f_{\text{isco}}^{-\frac{5}{3}}). \tag{35}$$

We see that Equation 35 is positively defined as $f < f_{\text{isco}}$.

We evaluate the second derivative of the phase as in [Cole et al., 2023]:

$$\ddot{\Phi}(f) = 4\pi^2 f \left(\frac{d\Phi(f)}{df} \right)^{-1} = \frac{384}{5} \frac{\pi^{\frac{14}{3}} G^{\frac{5}{3}} m_1 m_2}{M^{\frac{1}{3}} c^5} f^{\frac{11}{3}} \tag{36}$$

4 Results

4.1 Varying a single parameter

I present the results obtained by varying the parameters of Table 1. The figures I show display the dephasing, while the notebooks allow for evaluation of $h_0(f)$ and other quantities through the `Phase_Evaluation` class.

4.1.1 Accretion disk

Varying the highlighted parameters of the accretion disk yields the results shown in Figures 4 and 5.

Figure 4 shows an increase in the dephasing as the α value is increased. This might be because while keeping all other disk's parameters fixed, changing the value of α results in a different scale onto which the density is spread (or a different slope). This has the result of concentrating more or less matter into a given region thus providing different shrinking behaviours of the binary.

Figure 5 shows how increasing the density normalization (e.g. the density itself) of the accretion disk contributes to a higher dephasing. This is clearly because a higher density environment more strongly contributes to the shrinking of the binary distance, due to the higher torque exerted on the secondary mass.

4.1.2 Dark matter spike

Varying the highlighted parameters of the dark matter spike yields the results shown in Figures 6 and 7.

Figure 6 shows an increase in the dephasing as the γ_s value is increased. This might happen because while keeping all other spikes's parameters fixed, changing the value of γ_s results in a different scale onto which the density is spread (or a different slope). This has the result of concentrating more or less matter into a given region thus providing different shrinking behaviours.

Contributions to $\Delta\Phi(f)$
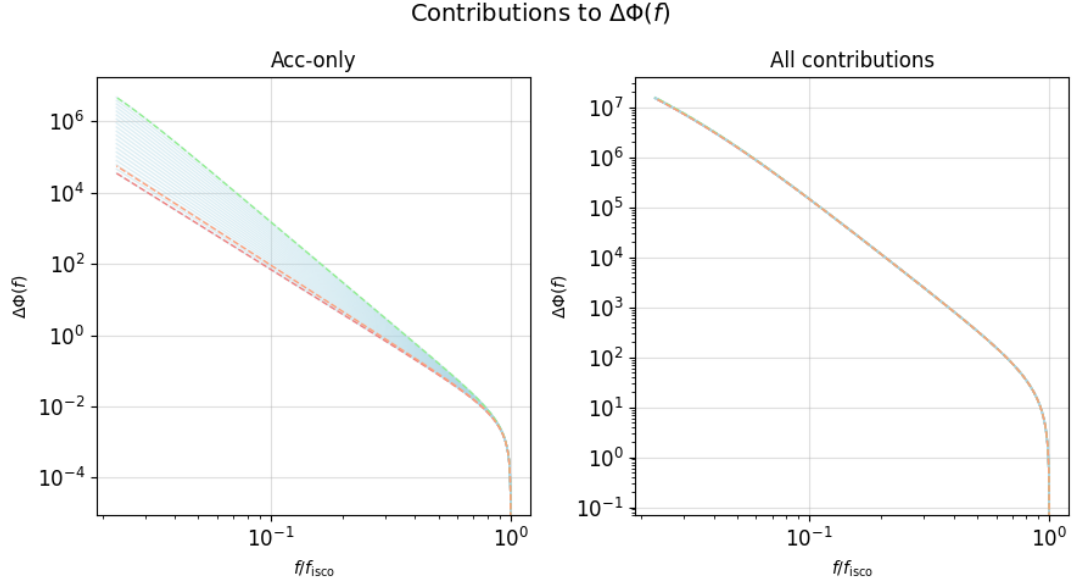
Figure 4: The change in the dephasing with different values for the α parameter. In pink we see the lower limits of the intervals highlighted in Table 1, in green the upper ones. The orange line instead is the reference value for each of the profiles, as per in [Cole et al., 2023].
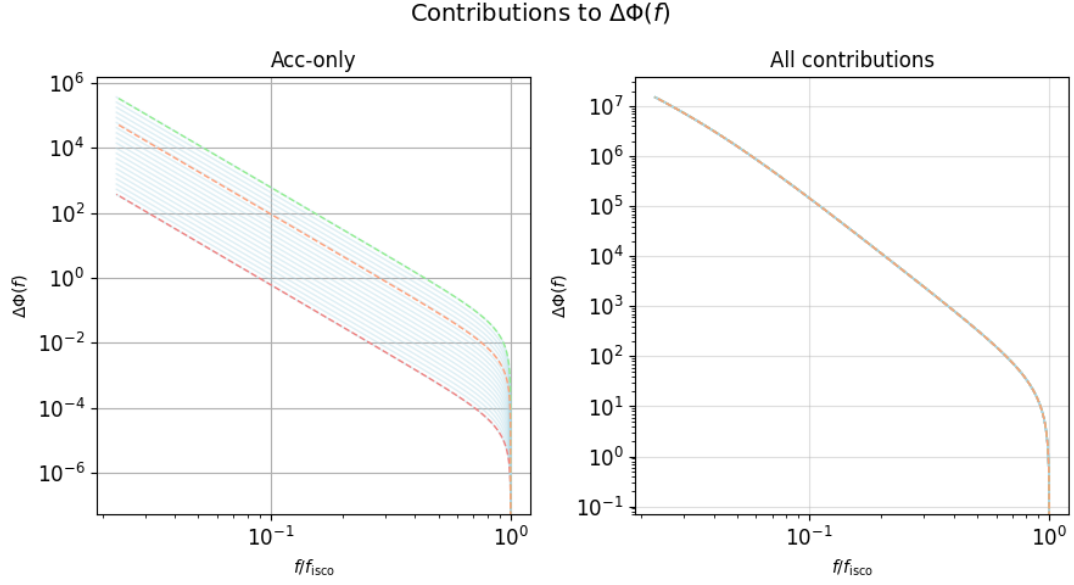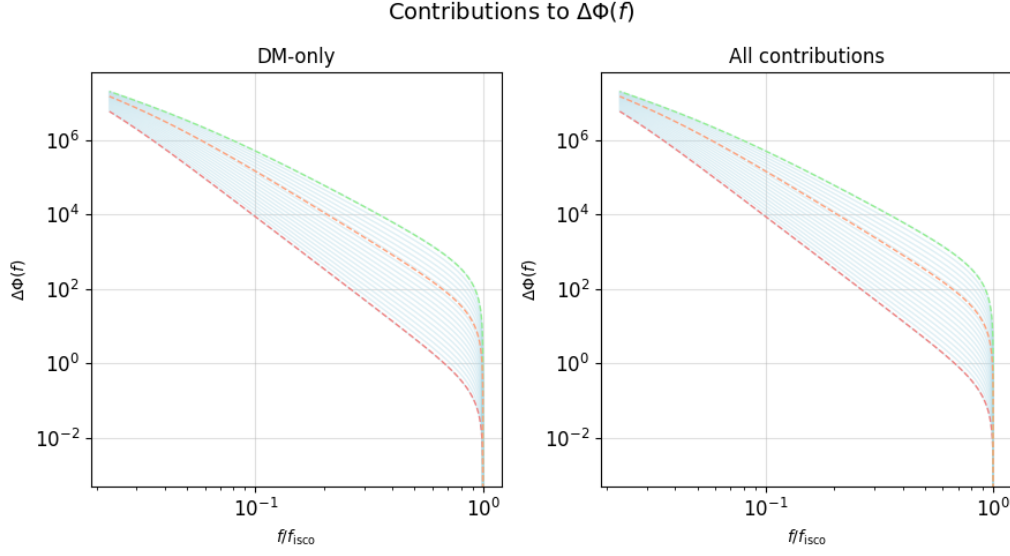
Contributions to $\Delta\Phi(f)$

Figure 5: The change in the dephasing with different values for the Σ_0 parameter. In pink we see the lower limits of the intervals highlighted in Table 1, in green the upper ones. The orange line instead is the reference value for each of the profiles, as per in [Cole et al., 2023].

Figure 6: The change in the dephasing with different values for the γ_s parameter. In pink we see the lower limits of the intervals highlighted in Table 1, in green the upper ones. The orange line instead is the reference value for each of the profiles, as per in [Cole et al., 2023].
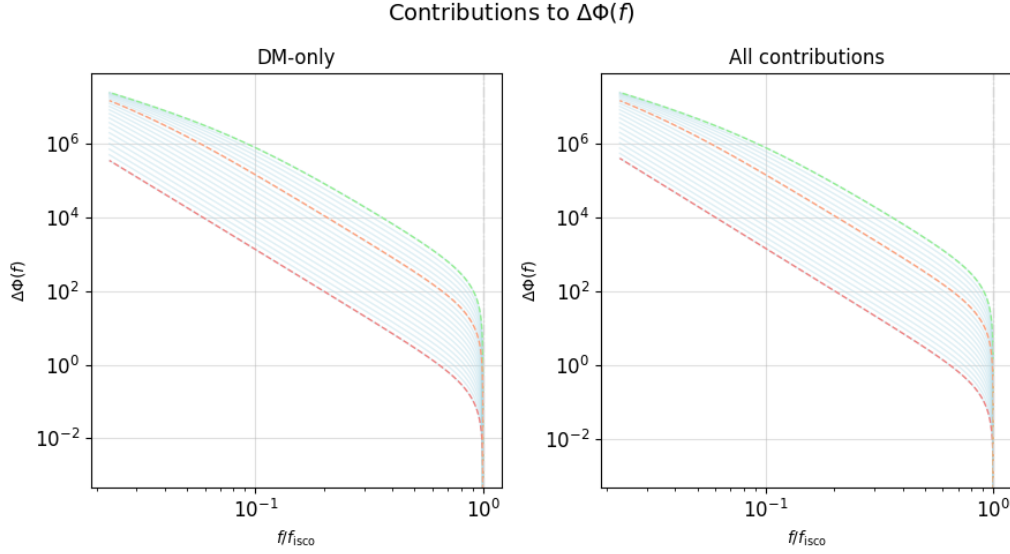

Figure 7: The change in the dephasing with different values for the ρ_s parameter. In pink we see the lower limits of the intervals highlighted in Table 1, in green the upper ones. The orange line instead is the reference value for each of the profiles, as per in [Cole et al., 2023].

Figure 7 shows how increasing the density normalization (e.g. the density itself) of the dark matter spike contributes to a higher dephasing. The dynamical friction is indeed much stronger if

11

the secondary object moves in a denser environment, contributing to a much higher effect on the dephasing.

4.1.3 Central object mass

Varying the mass value of the central intermediate black hole yields the results shown in Figure 8.
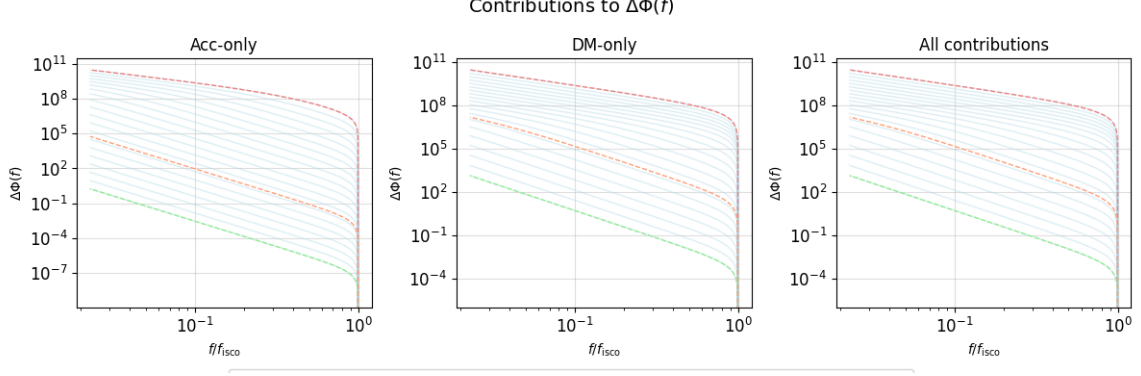

Figure 8: The change in the dephasing with different values for the m_1 parameter. In pink we see the lower limits of the intervals highlighted in Table 1, in green the upper ones. The orange line instead is the reference value for each of the profiles, as per in [Cole et al., 2023].

Figure 8 shows how a larger mass results in a smaller dephasing, if we keep all other parameters fixed. This might happen because a larger central mass results in a larger pull on the secondary object, which shrinks faster. This behaviour is seen in both the vacuum and environmental dephasing.

4.2 Varying two parameters at a time

In this section I report the graphs adopted to study the dephasing based on varying two parameters at a time. I chose to initially vary both densities of the DM spike and accretion disk ρ_s and Σ_0, and then the two slopes α and γ_s. The results are respectively shown in Figure 10 and Figure 11, for different points of the dephasing $\Delta\Phi$. A general scheme of how the two plots should be read is shown in Figure 9.

Both Figure 10 and Figure 11 show that in the proximity of the f_{ISCO} the dephasing is very flat, probably indistinguishable it from the vacuum case. Subsequently we must move away from the ISCO frequency, to expect a higher detection chance (see the lower right part of both graphs). The dark matter profile is dominant, meaning that any high valued dephasing can be attributed to its variations rather than the presence of the accretion disk.

An important analysis to carry out consists into tuning down the dark matter spike normalization to the point where the accretion disk is more visible, and at the same time setting the condition of Equation 6.
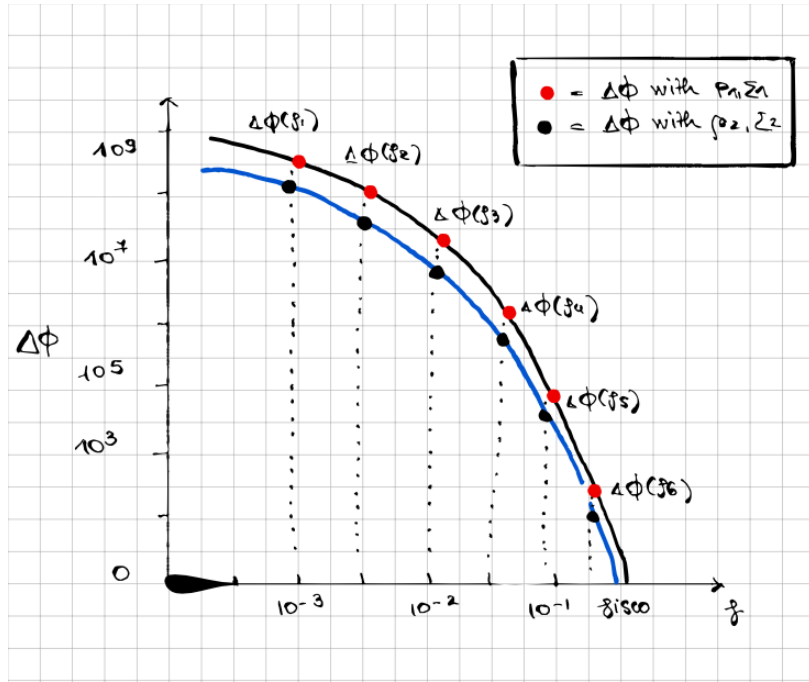
Figure 9: The general idea for interpreting the density plots shown in Figure 10, and figure 11. For a single couple of parameters (here Σ_0 and ρ_s) there is a specific value of the dephasing, corresponding to one of the cells. Varying one parameter with respect to the other and vice versa, keeping that one point fixed, is what allows to produce multiple plots at a fixed frequency.
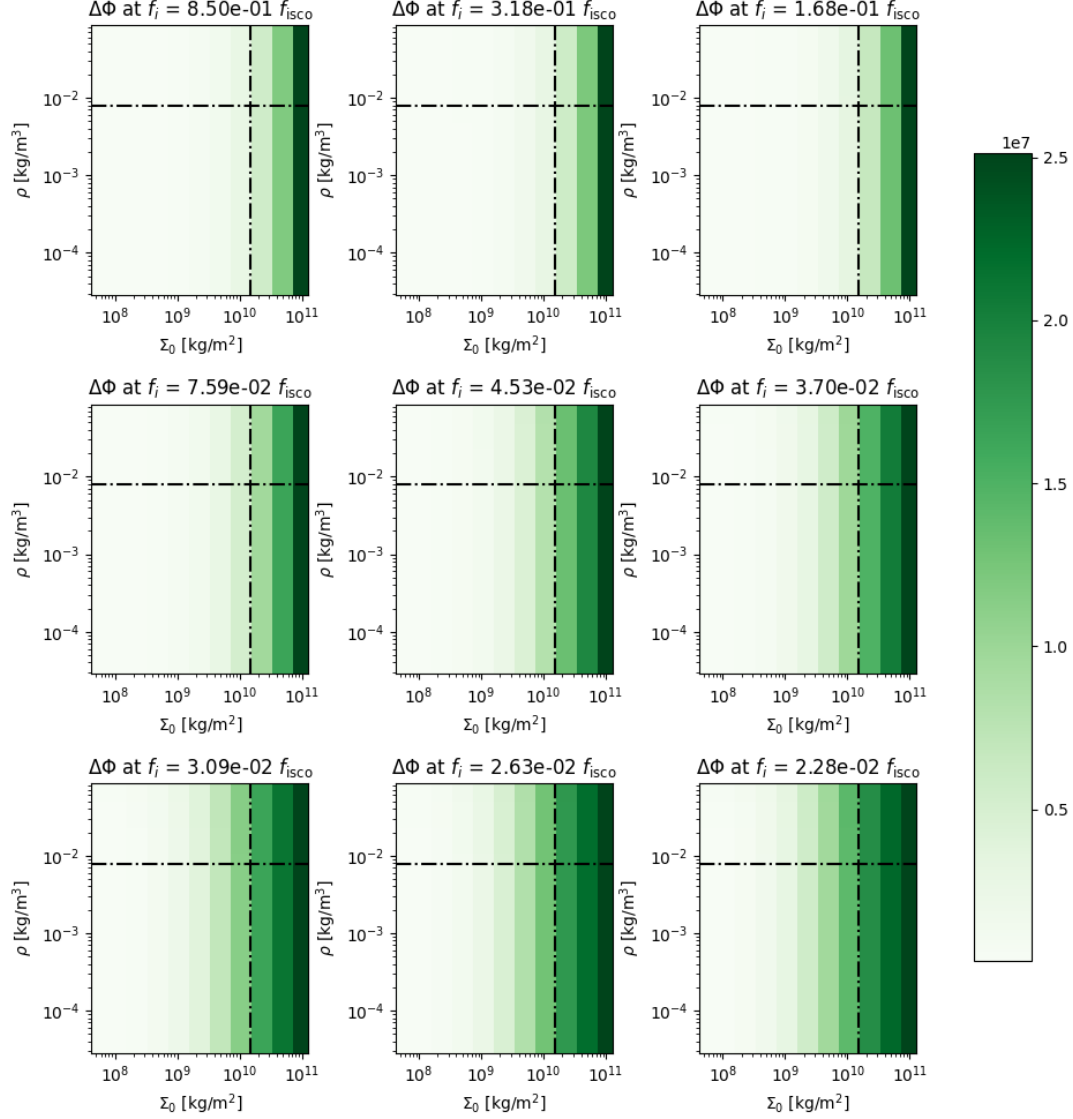
Figure 10: The different results obtained for $\Delta\Phi$, varying the normalization densities of the environments, evaluated at the same frequency point. We see how changing these parameters can strongly affect the evaluation at a single point of the dephasing. In black I report the reference values of Table 1.

14

Figure 11: The different results obtained for $\Delta\Phi$, varying the density slopes of the environments, evaluated at the same frequency point. We see how changing these parameters can strongly affect the evaluation at a single point of the dephasing. In black I report the reference values of Table 1.
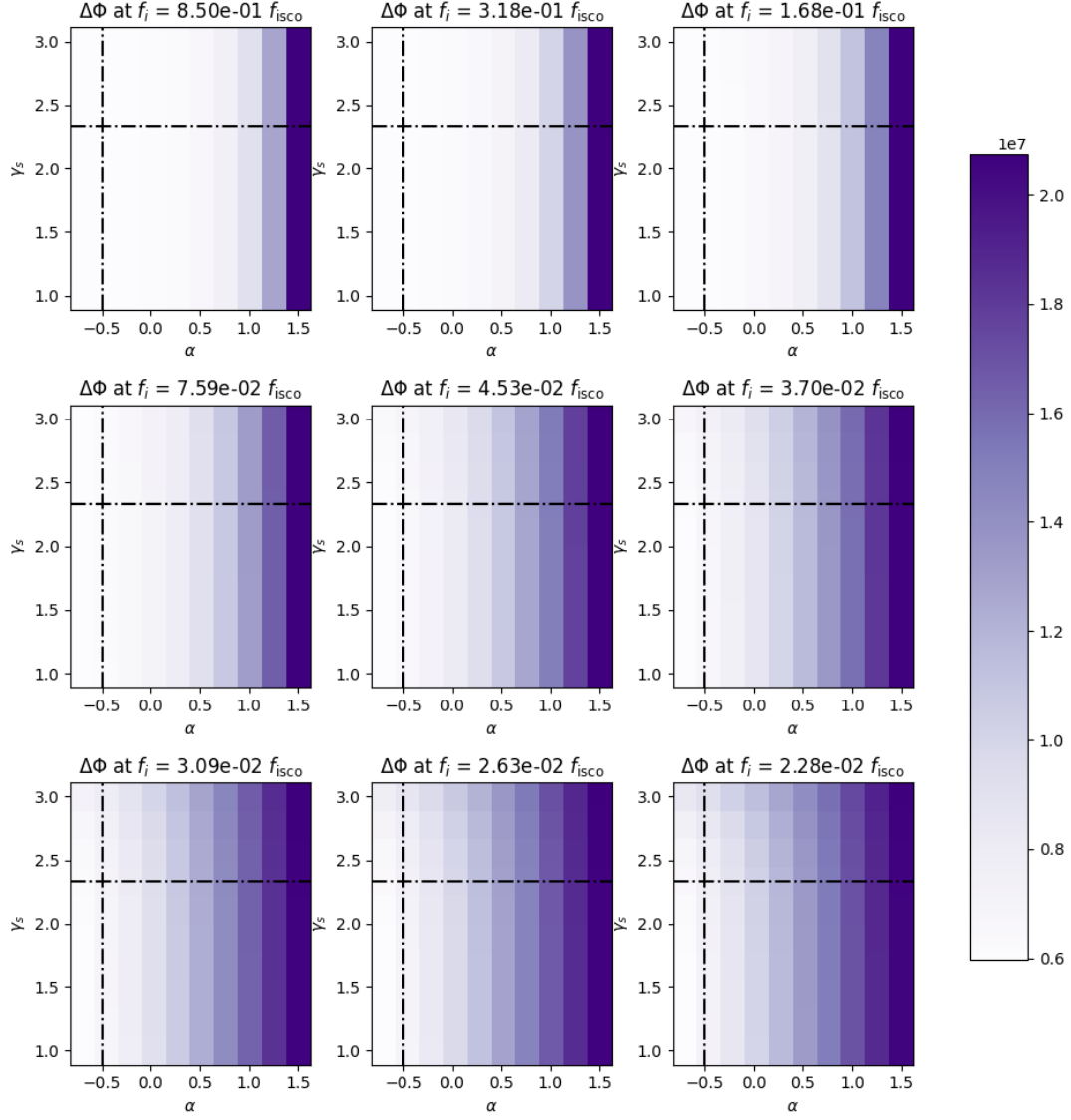
4.2.1 Dark matter benchmark

In this paragraph I report the result I obtained by tuning down the dark matter density normalization (**note!**: in the static profile). This has proved to be the most relevant when it comes to the dephasing measurement, if not dominant. The goal is to lower it as much as possible to find, fixing all other parameters as in Table 2.
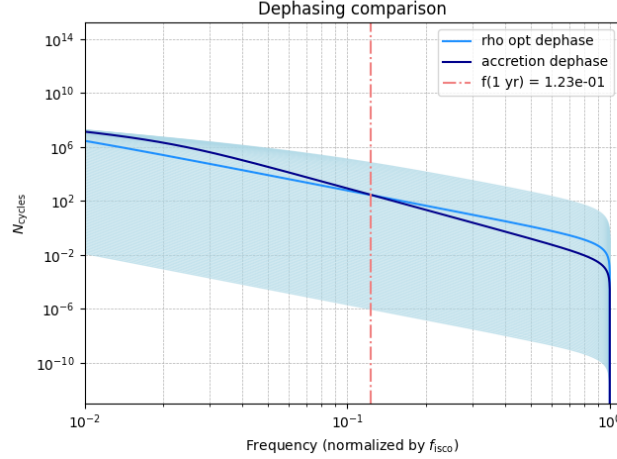

Figure 12: The comparison between the dephasing obtained for an accretion-only environment VS a dark matter-only environment. In the plot I also report the value of the frequency assoiated to $t_{\text{coal}} = 1$ yr.

The goal is to compare the dephasing obtained for the accretion-only case and the dark matter-only case, and see for which normalization value the two have the same strength at a fixed frequency, which I chose to be the one where $t_{\text{coal}} = 1$ yr. To extract the latter we use:

$$t_{\text{coal}} = \int_{f}^{f_{\text{isco}}} \frac{dt}{df} df. \tag{37}$$

Comparing 100 possible realizations of the dephasing due to a varying parameter ρ_6, we find the result in Figure 12. The result seems to indicate that the optimal parameter is:

$$\rho_{6,\text{opt}} = 2.7825594 \cdot 10^{15} \frac{M_\odot}{\text{pc}^3} \tag{38}$$

4.3 Substituting the effective dark matter profile

An important aspect of the study is to include models that better encapsule the real behavior of the environment. Indeed a dynamically evolving dark matter profile that takes into account the particles depletion by the inspiral will probably better describe what happens rather than a static, non-evolving density profile. We can include $\dot{r}_{\text{eff,dm}}$ instead of the static one in the combined environments case. In some models, the resulting dephasing seems to go negative at a certain cut frequency. I here report two of the models I tested and their respective results: Table 3 reports the values I set to find the results of Figure 13. , while Table 4 reports the values I set to find the results of Figure 14.
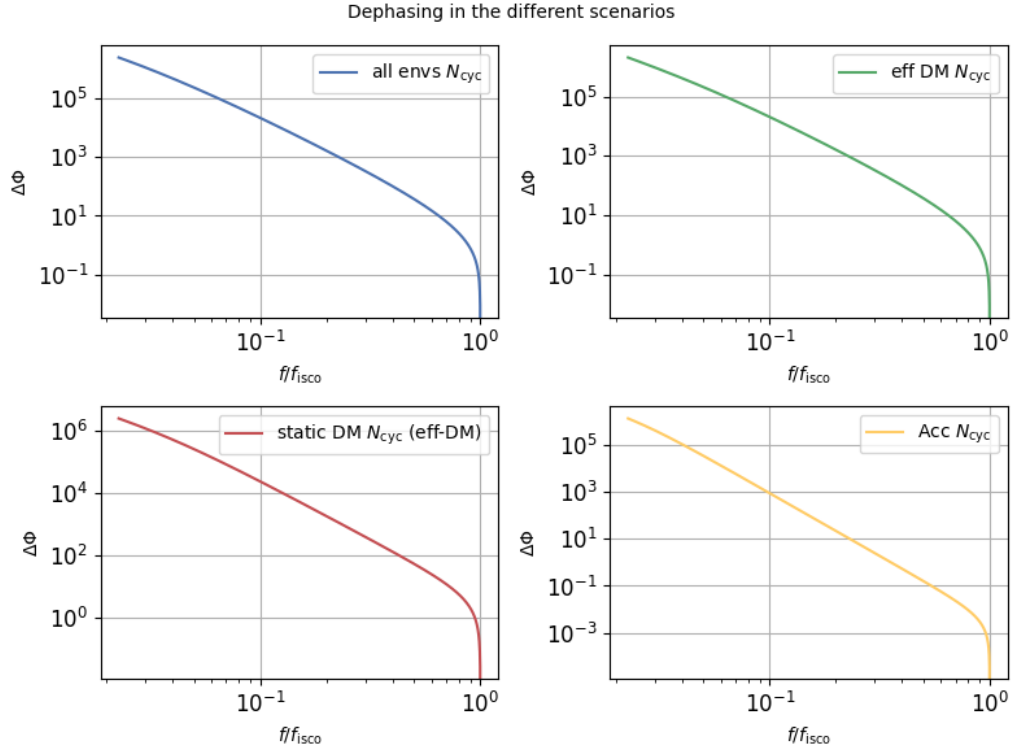
Figure 13: The dephasings obtained through the numerical integration with the parameters of Table 3.
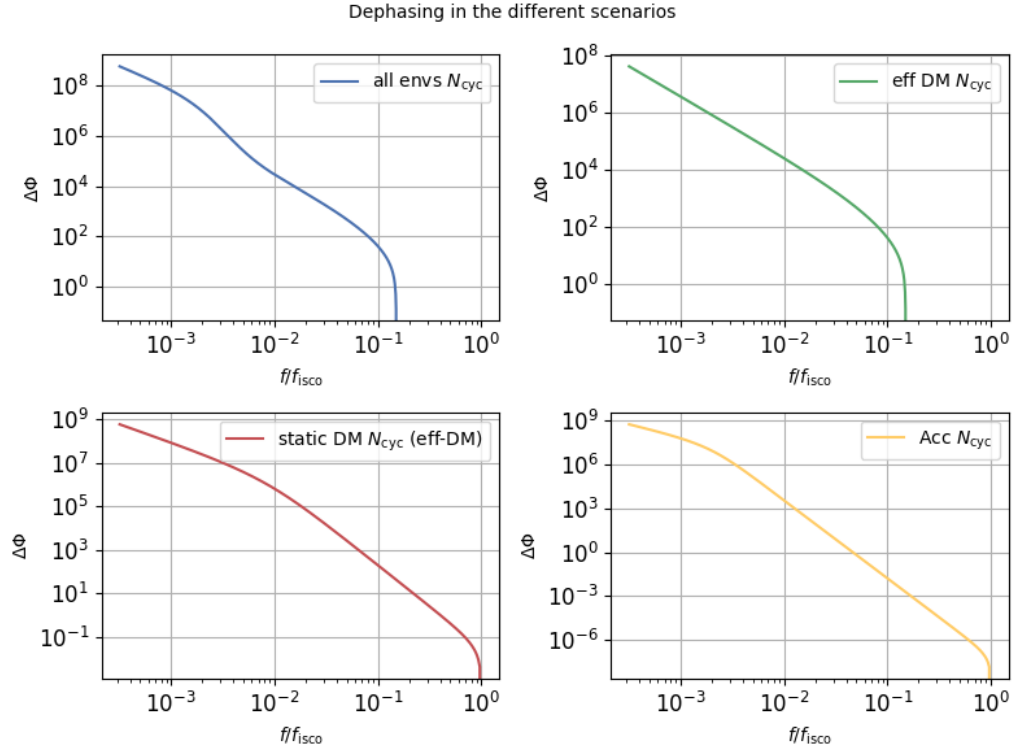
Figure 14: The dephasing obtained through the numerical integration with the parameters of Table 4. We see how at a certain frequency the values go negative if dark matter is present. What is happening here?

Reference values tables

4.4 Varying one parameter/ two parameters at a time

Benchmark parameters	values
$m_1 \ [M_\odot]$	$[10^3, 10^6]$
$m_2 \ [M_\odot]$	10
$\mathcal{M}$	100
$\Sigma_0 \ [\mathrm{kg/m^2}]$	$[10^8, 10^{11}]$
α	$[-0.7, 1.5]$
$log(\Lambda)$	$\sqrt{m_2/m_1}$
γ_s	$[1, 3]$
$\rho_6 \ [M_\odot/\mathrm{pc^3}]$	$[10^{15}, 10^{18}]$
ϵ_v	0.58
$D \ [\mathrm{Gpc}]$	4

Table 1: The parameters I choose for Section 4.1, color-coded as: the binary, accretion disk, and dark matter spike parameters. I highlighted the parameters I kept fixed in the analysis, with the red color.

4.5 Dark matter benchmark

Benchmark parameters	values
$m_1 \ [M_\odot]$	10^5
$m_2 \ [M_\odot]$	10
$\mathcal{M}$	100
$\Sigma_0 \ [\mathrm{kg/m^2}]$	$1.5 \ 10^{10}$
α	-0.5
$\log(\Lambda)$	$\sqrt{m_2/m_1}$
γ_s	$\frac{7}{3}$
$\rho_6 \ [M_\odot/\mathrm{pc^3}]$	$[10^7, 10^{18}]$
ϵ_v	0.58
$D \ [\mathrm{Gpc}]$	4

Table 2: The parameters I choose for my model, color-coded as: the binary, accretion disk, and dark matter spike parameters. Note in red the values grid I chose for the ρ_6 parameter.

4.6 Effective DM model comparison

Benchmark parameters	values
m_1 [$M_\odot$]	10^5
m_2 [$M_\odot$]	10
$\mathcal{M}$	100
Σ_0 [kg/m^2]	$1.5\ 10^{10}$
α	-0.5
$\log(\Lambda)$	$\sqrt{m_2/m_1}$
γ_s	$\frac{7}{3}$
ρ_6 [$M_\odot$/pc^3]	$1.17\ 10^{17}$
ϵ_v	0.58
D [Gpc]	4

Table 3: The parameters I choose for my model, color-coded as: the binary, accretion disk, and dark matter spike parameters.

Benchmark parameters	values
m_1 [$M_\odot$]	$1.4\ 10^3$
m_2 [$M_\odot$]	1.4
$\mathcal{M}$	100
Σ_0 [kg/m^2]	$1.5\ 10^{10}$
α	-0.5
$log(\Lambda)$	$\sqrt{m_2/m_1}$
γ_s	$\frac{7}{3}$
ρ_6 [$M_\odot$/pc^3]	$7.0.78 10^{15}$
ϵ_v	0.58
D [Gpc]	4

Table 4: The parameters I choose for my model, color-coded as: the binary, accretion disk, and dark matter spike parameters.

Useful links

- https://github.com/bradkav/HaloFeedback

- https://github.com/nicolegrillo/BinaryEvolution

References

[Binney and Tremaine, 1987] Binney, J. and Tremaine, S. (1987). *Galactic dynamics*.

[Chandrasekhar, 1943] Chandrasekhar, S. (1943). Dynamical Friction. I. General Considerations: the Coefficient of Dynamical Friction. , 97:255.

[Cole et al., 2023] Cole, P. S., Bertone, G., Coogan, A., Gaggero, D., Karydas, T., Kavanagh, B. J., Spieksma, T. F. M., and Tomaselli, G. M. (2023). Distinguishing environmental effects on binary black hole gravitational waveforms. *Nature Astronomy*, 7:943–950.

[Derdzinski et al., 2020] Derdzinski, A., D'Orazio, D., Duffell, P., Haiman, Z., and MacFadyen, A. (2020). Evolution of gas disc–embedded intermediate mass ratio inspirals in the LISA band. *Monthly Notices of the Royal Astronomical Society*, 501(3):3540–3557.

[Kavanagh et al., 2020] Kavanagh, B. J., Nichols, D. A., Bertone, G., and Gaggero, D. (2020). Detecting dark matter around black holes with gravitational waves: Effects of dark-matter dynamics on the gravitational waveform. , 102(8):083006.

[Tanaka et al., 2002] Tanaka, H., Takeuchi, T., and Ward, W. R. (2002). Three-dimensional interaction between a planet and an isothermal gaseous disk. i. corotation and lindblad torques and planet migration. *The Astrophysical Journal*, 565(2):1257.